

Learning operando impedance function for battery health with aging-aware equivalent circuit model

Zihao Zhou*, Antti Aitio, David Howey**

* *Engineering Science Department, University of Oxford, United Kingdom (e-mail: zihao.zhou@eng.ox.ac.uk).*

** *Engineering Science Department, University of Oxford, United Kingdom (e-mail: david.howey@eng.ox.ac.uk).*

Abstract: The wide usage of Lithium-ion batteries (LIBs) requires a deep understanding about battery health. Estimation of battery state-of-health (SOH) is a crucial but yet still challenging task. Pure model-based methods may suffer from inaccuracy and instability of parameter estimations in lifelong aging. While pure data-driven methods rely heavily on quality and quantity of training set, causing lack of generality when extrapolating into unseen cases. In this paper, we propose an aging-aware equivalent circuit model (ECM), which combines model-based and data-driven techniques for SOH estimation. Gaussian process (GP) regression is incorporated in ECM to modelling parameters dependency on operating condition and aging time. The state space formulation of GP is used to enable a computationally efficient co-estimation framework of both parameters and states. Samples from two Open datasets are used to validate model performance, which gives accurate estimation for capacity and impedance. The learnt impedance function can be lined to the shape change of open circuit voltage (OCV) versus SOC curve and thus providing a way to further estimate changes of differential voltage (dV/dQ) curves.

Keywords: battery SOH estimation, Gaussian process regression, state space model, equivalent circuit model.

1. INTRODUCTION

Lithium-ion batteries (LIBs) have played an important role in transitioning to a carbon-neutral society. Due to their relative longevity and high energy density, the demand for LIBs systems is rapidly increasing in power grid, electric vehicles (EV) and home energy storage systems (Tsiropoulos et al., 2018). One of the most crucial challenges for using LIBs locates in estimating the state of health (SOH). An accurate estimation for battery SOH improves battery lifetime, system safety, timing of warranty and maintenance. Despite the first life usage scenarios, many studies (Hua et al., 2021; Shahjalal et al., 2022; Zhou et al., 2020) have address the importance of properly dealing with retired LIBs, which will increase drastically in near future. Estimating the evolution trend of SOH from historical usage data will enable additional possibilities for battery residual value evaluation.

The commonly use indicator—discharge capacity normally requires the battery going through a low rate constant current discharge from 100% to 0% state of charge (SOC). Due to the time consuming nature for getting ground truth discharge capacity, it is often not available in real world applications, thus, extensive studies have been done on capacity estimation (Berecibar et al., 2016; Wang et al., 2020). These methods are usually categorised into model-driven and data-driven approaches. Model-driven methods use a specific battery model (either electrochemical model

or equivalent circuit model), and the model parameters need to be updated (i.e. repeatedly fitted) along battery aging (Plett, 2004; Gao et al., 2021). While electrochemical models often needs half-cell test data for parameterization and tend to suffer from parameter identifiability problems (Lu et al., 2021; Miguel et al., 2021). Equivalent-circuit models, which have relatively less number of model parameters are often favored in this case. Recursive state estimation techniques, such as extended Kalman filter (Wassiliadis et al., 2018) and particle filter (Wei et al., 2017) are often adopted for co-estimation of model states and parameters. Discharge capacity as one of the most important model parameters is thus tracked along battery usage.

On the other hand, data-driven methods for capacity estimation try to map carefully selected features to corresponding capacity values (Li et al., 2019). Many useful features are extracted from certain area of battery raw signals (voltage/current/temperature) (Severson et al., 2019; Greenbank and Howey, 2021). Also, usage related features (Li et al., 2024) are shown to be effective especially when dealing with batteries undergoing different cycling. Then, machine learning models such as support vector machine (Feng et al., 2019), random forest (Li et al., 2018), neural networks (Li et al., 2021) and Gaussian process (Richardson et al., 2018) have been used to capture the mapping relationship between these features and capacity. Depending on the choice of inputs, these data-driven models can

be used for either estimating present capacity or predicting the future SOH. If the learnt mapping is between feature and future capacity values, these models can be directly used for forecasting. The performance of machine learning models is largely influenced by quantity and accuracy of collected labels (i.e ground truth capacity).

Moreover, capacity decay only represents one aspect of battery degradation. while the increasing impedance also plays an essential role when consider battery health (Fu et al., 2021). Compared to capacity, impedance values are much easier to estimate from different kinds of cycling data, which means more available labels for estimation. Especially, from studies (Pozzato et al., 2023; Sulzer et al., 2021) on field data, capacity values are pointed to be hard to get and not enough to describe battery performance. It suggests the advantages and large potential for estimating the operando impedance as a health indicator for battery. Many SOH estimation works treat impedance as a scalar or a look-up table need to be calibrated in standard reference test (Plett, 2004; Locorotondo et al., 2021). However, many experiment works show impedance does change with operating conditions (Waag et al., 2013; Schönleber et al., 2017). Furthermore, health metrics related to different degradation modes, such as lost of lithium-ion inventory (LLI), lost of active material from both electrodes (LAM_n, LAM_p) often enables deeper understanding of battery aging (Dubarry et al., 2012; Dubarry and Anseán, 2022).

In this work, we propose an aging-aware equivalent circuit model and use it to estimate both capacity and operando impedance from cycling data. The model parameters (capacity and impedance) are described as functions of aging time and operating conditions (i.e. SOC and the applied current). Specifically, we use Gaussian process regression to modelling the operating condition and aging time dependency of impedance, as well as the aging dependency of capacity. The estimation results for both capacity and operando impedance function reveal rich battery aging information. It is found that the learnt impedance function can be lined to the shape change of open circuit voltage (OCV) versus SOC curve and thus providing a way to further estimate changes of differential voltage (dV/dQ) curves. By formulating Gaussian process into its state space form, the GP subsystems are combined into ECM, thus creating a nonlinear system. The battery states and state-dependent circuit parameters are co-estimated based on extended Kalman filter. This framework scales linearly with the time step of input-output data and only requires an initial-of-life OCV-SOC relationship. Open source data of two batteries (Li et al., 2024; Jöst et al., 2021) with different cycling conditions are used to validate model performance. Our method not only gives accurate estimation for capacity and impedance, but also enables a deeper analysis for battery degradation.

2. METHODOLOGY

2.1 State space formulation of Gaussian process

A Gaussian process (GP) is defined as a distribution of functions over input \mathbf{x} , which is characterised by a mean and a covariance, while the covariance is defined by the selected kernel function $k(\mathbf{x}, \mathbf{x}')$,

$$f(\mathbf{x}) \sim \mathcal{GP}(m(\mathbf{x}), k(\mathbf{x}, \mathbf{x}')) \quad (1)$$

When this input includes both locations in space and time $\mathbf{x} = (s, t)$, it is often called a spatial-temporal Gaussian process.

$$f(s, t) \sim \mathcal{GP}(m(s, t), k((s, t), (s', t'))) \quad (2)$$

Without loss of generality, the mean function $m(\mathbf{x})$ is set to zero. And by assuming a measurement noise term ϵ , the mapping between \mathbf{x} and \mathbf{y} can be expressed as,

$$\mathbf{y} = f(\mathbf{x}) + \epsilon, \epsilon \sim \mathcal{N}(0, \sigma_n^2 \mathbf{I}) \quad (3)$$

The aim is to find the posterior predictive distribution for test samples \mathbf{X}^* based on our observation on a labeled training set of input-output pairs $\mathcal{D} = \{(\mathbf{x}_i, y_i)\}_{i=1}^N$, the analytical solution is given by (Williams and Rasmussen, 2006),

$$p(\mathbf{y}^* | \mathbf{X}^*, \mathbf{X}, \mathbf{y}) = \mathcal{N}(\mathbf{y}^* | \mathbf{m}^*, \Sigma^*) \quad (4)$$

where,

$$\begin{aligned} \mathbf{m}^* &= \mathbf{K}_{X, *}^T [\mathbf{K}_X + \sigma_n^2 \mathbf{I}]^{-1} \mathbf{y} \\ \Sigma^* &= \mathbf{K}_{*, *} - \mathbf{K}_{X, *}^T [\mathbf{K}_X + \sigma_n^2 \mathbf{I}]^{-1} \mathbf{K}_{X, *} \end{aligned} \quad (5)$$

And kernel matrices are simplified as $\mathbf{K}_X = k(\mathbf{X}, \mathbf{X})$, $\mathbf{K}_{X, *} = k(\mathbf{X}, \mathbf{X}^*)$. For a zero-mean GP, the model is defined by training data and the selected kernel function $k(\mathbf{x}, \mathbf{x}')$. The negative log maximum likelihood estimates (NLML) of kernel hyper-parameters θ is given by,

$$\begin{aligned} \text{NLML} &= -\log p(\mathbf{y} | \mathbf{X}, \theta) = \\ &= -\frac{1}{2} \mathbf{y}^T [\mathbf{K}_X - \sigma_n^2 \mathbf{I}]^{-1} \mathbf{y} - \frac{1}{2} \log |\mathbf{K}_X| - \frac{n}{2} \log 2\pi \end{aligned} \quad (6)$$

One major problem that limit the usage of GP is the poor computational scaling. The inversion of an $N \times N$ matrix in both eqn. 5 and 6 scales computationally $\mathcal{O}(n^3)$. Here, we adopt a state-space formulation of GP, which scales linearly with time steps $\mathcal{O}(n)$.

Proposed by Särkkä et al. (Sarkka et al., 2013) and Solin (Solin et al., 2016), the state space formulation interprets a spatial-temporal Gaussian process $f(s, t)$ as the solution to a linear time-invariant stochastic partial differential equation (LTI-SPDE).

$$\begin{aligned} \frac{\partial \mathbf{x}(s, t)}{\partial t} &= \mathcal{F} \mathbf{x}(s, t) + \mathbf{L} \omega(s, t) \\ \mathbf{y}_t &= \mathcal{H}_t \mathbf{x}(s, t) + \epsilon_t, \quad \epsilon \sim \mathcal{N}(0, \sigma_n^2) \end{aligned} \quad (7)$$

where, for a finite collection of spatial points of interest $\{s_i\}_i^{n_s}$, the states becomes,

$$\begin{aligned} \mathbf{x}(s, t) &= [\mathbf{x}(s_1, t), \mathbf{x}(s_2, t), \dots, \mathbf{x}(s_{n_s}, t)]^T \\ \mathbf{x}(s_i, t) &= \left[f(s_i, t), \frac{df(s_i, t)}{dt}, \dots, \frac{df(s_i, t)^{m-1}}{dt^{m-1}} \right]^T \end{aligned} \quad (8)$$

\mathcal{F} and \mathcal{H} are linear operators, \mathbf{L} is a dispersion matrix, and $\omega(\mathbf{x}, t)$ is spatially resolved white noise process decided by the spatial kernel. The mathematical foundation lays on the Wiener-Khinchin theorem (Cohen, 1998), which indicates that the GP kernel covariance matrix and the spectral density of a solution process for LTI-SPDE form a Fourier transform pair. For a specific spatial point s_i , all the $m-1$ orders time gradient information are maintained and propagated into future. While this propagation is operated for all n_s spatial points. The exact value for m is decided by the selected time kernel. Intuitively, one can

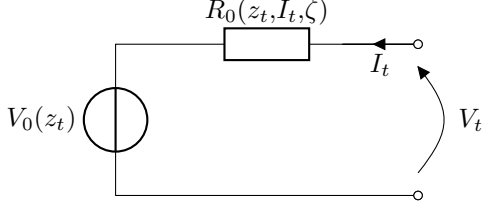


Fig. 1. Equivalent circuit model for Li-ion battery

view it as constructing a LTI system which takes a white noise process as input, and its output process is effectively the desired Gaussian process.

In order to further simplify linear operators into matrix, one essential assumption is the kernel separability,

$$k((s, t), (s', t')) = k(s, s') k(t, t') \quad (9)$$

Under this assumption, \mathcal{F} and \mathcal{H} will become constant matrices \mathbf{F} and \mathbf{H} . As a result, a kernel function of GP may be directly mapped to \mathbf{F} , \mathbf{H} and $\omega(s, t)$, while these matrices defined a corresponding LTI system. The practical implementation of eqn. 7 needs to transform it into its corresponding discretization form.

$$\begin{aligned} \mathbf{x}_k &= \mathbf{A}_{k-1} \mathbf{x}_{k-1} + \mathbf{w}_{k-1} \\ y_k &= \mathbf{H}_k \mathbf{x}_k + v_k, \quad v_k \sim \mathcal{N}(0, \sigma_n^2) \end{aligned} \quad (10)$$

where $\mathbf{x}_k = [\mathbf{x}_{s_1, k}, \mathbf{x}_{s_2, k}, \dots, \mathbf{x}_{s_{n_s}, k}]^\top$ representing a value vector along all n_s space locations at time step t_k , and $\mathbf{A}_k = \exp(\Delta t_k \mathbf{I}_{n_s} \otimes \mathbf{F})$ means a matrix exponential on \mathbf{F} and time interval $\Delta t_k = t_{k+1} - t_k$. The kronecker product here comes from space discretization. Each space location is propagate in time at its own while their space relationship is captured by the process noise term \mathbf{w}_{k-1} . \mathbf{w}_{k-1} is a zero-mean multivariate GP on the n_s space locations with covariance function expressed as,

$$\begin{aligned} \mathbf{w}_{k-1} &\sim \mathcal{GP}(\mathbf{0}, \mathbf{K}_s \otimes w_{k-1}) \\ w_{k-1} &= \int_0^{\Delta t_k} \mathbf{A}_{k-1} \mathbf{L} \mathbf{Q}_c \mathbf{L}^\top \mathbf{A}_{k-1}^\top d\tau \end{aligned} \quad (11)$$

where \mathbf{K}_s is the $n_s \times n_s$ covariance matrix of space kernel $k(s, s')$ on n_s locations. And \mathbf{Q}_c here is decided by time kernel $k(t, t')$ as math combination of kernel hyper-parameters.

Once the GP is formulated as discrete time LTI system, both the estimation of posterior predictive distribution in eqn. 5 and the hyper-parameter NLML in eqn. 6 can be achieved recursively using Kalman filter and Rauch-Tung-Striebel smoother (Särkkä and Svensson, 2023), which enables a linear time complexity for model forward running.

2.2 Incorporate Gaussian process into circuit model

As shown in Fig. 1, a simple equivalent circuit model (ECM) is used for modelling battery dynamics. The corresponding math formulation is given as,

$$\begin{aligned} V_t &= V_0(z_t) + R_0(z_t, I_t, \zeta) I_t \\ \frac{dz_t}{dt} &= I_t Q^{-1}(\zeta) \end{aligned} \quad (12)$$

where, z_t is SOC, I_t is the applied current, $V_0(z_t)$ represents the given OCV-SOC curve, which is often given at initial of life and assumed to be fixed along cycling. Two

time scales are included in this ECM, one is the operating time scale (t), which is often in seconds level. Another is the life-long aging time scale (ζ), which can vary from days to months depending on usage. For simplicity, we use one variable to denote operating conditions,

$$\mathbf{s}_t = [z_t, I_t]^\top \quad (13)$$

The capacity term Q^{-1} is modeled as a GP over ζ , while the impedance term R_0 is modeled as a GP over \mathbf{s}_t and ζ ,

$$\begin{aligned} Q^{-1}(\zeta) &\sim \mathcal{GP}(m(\zeta), k(\zeta, \zeta')) \\ R_0(\mathbf{s}_t, \zeta) &\sim \mathcal{GP}(m(\mathbf{s}_t, \zeta), k((\mathbf{s}_t, \zeta), (\mathbf{s}_t', \zeta'))) \end{aligned} \quad (14)$$

Given the nonzero nature of impedance and capacity, instead of directly modelling R_0 and Q , we choose to model it as an affine transformation of a zero-mean GP, which is equivalent to setting a nonzero prior mean for impedance and capacity. Specifically, Eqn. 14 are further written as,

$$\begin{aligned} Q^{-1}(\zeta) &= q_0(1 + q(\zeta)) \\ R_0(\mathbf{s}_t, \zeta) &= r_0(1 + r(\mathbf{s}_t, \zeta)) \\ q(\zeta) &\sim \mathcal{GP}(0, k(\zeta, \zeta')) \\ r(\mathbf{s}_t, \zeta) &\sim \mathcal{GP}(0, k((\mathbf{s}_t, \zeta), (\mathbf{s}_t', \zeta'))) \end{aligned} \quad (15)$$

where constants r_0, q_0 reflects our prior expectation for the values of R_0, Q^{-1} respectively. In practice, they can be set to the corresponding begin-of-life (BOL) values. As a Gaussian distribution remains Gaussian under arbitrary affine transformation, R_0 and Q^{-1} are still GPs.

Follow the kernel separability assumption, the operating condition dependency on \mathbf{s}_t and the life-long aging dependency are modelled with different kernels,

$$k((\mathbf{s}_t, \zeta), (\mathbf{s}_t', \zeta')) = k_{\text{Matern}32}(\mathbf{s}_t, \mathbf{s}_t') k_{\text{WV}}(\zeta, \zeta') \quad (16)$$

where, k_{WV} and k_{Mat} represent Wiener velocity (WV) kernel and Matern ($\nu = 3/2$) kernel and respectively.

$$\begin{aligned} k_{\text{WV}}(\zeta, \zeta') &= \sigma_\zeta^2 \left(\frac{\min^3(\zeta, \zeta')}{3} + |\zeta - \zeta'| \frac{\min^2(\zeta, \zeta')}{2} \right) \\ k_{\text{Mat}}(\mathbf{s}_t, \mathbf{s}_t') &= \sigma_s^2 (1 + \sqrt{3}d) \exp(-\sqrt{3}d) \\ d^2 &= |\mathbf{s}_t - \mathbf{s}_t'|^\top \begin{bmatrix} l_z^{-2} & 0 \\ 0 & l_I^{-2} \end{bmatrix} |\mathbf{s}_t - \mathbf{s}_t'| \end{aligned} \quad (17)$$

While stationary kernels converge back to the mean on long term extrapolation, the WV kernel is a non-stationary kernel which is more suitable for extrapolating aging trend into future.

As shown in Fig. 2, the battery operating dynamics (ECM) and battery aging dynamics (GPs) are evolving in two different time scales. While the ECM state (z) changes in seconds during cycling (t), the GPs states (Q^{-1}, R_0) may changes in weeks/months along cell aging (ζ). To clarify notations, we use indexes i and j to denote the discrete time points for t and ζ respectively.

The state propagation for ECM can be expressed as,

$$z_i = z_{i-1} - Q^{-1} I_i \Delta t_i \quad (18)$$

The state propagation for GPs can be written as,

$$\begin{aligned} \mathbf{x}_{Q^{-1}, j} &= \exp(\Delta \zeta_j \mathbf{F}_{\text{WV}}) \mathbf{x}_{Q^{-1}, j-1} + w_{j-1} \\ \mathbf{x}_{R_0, j} &= \exp(\Delta \zeta_j \mathbf{L}_{n_s} \otimes \mathbf{F}_{\text{WV}}) \mathbf{x}_{R_0, j-1} + \mathbf{w}_{j-1} \end{aligned} \quad (19)$$

where, for the selected WV kernel, $\mathbf{F}_{\text{WV}} = \begin{bmatrix} 0 & 1 \\ 0 & 0 \end{bmatrix}$. $\Delta \zeta_j$ represents the discrete time interval in the lifelong aging

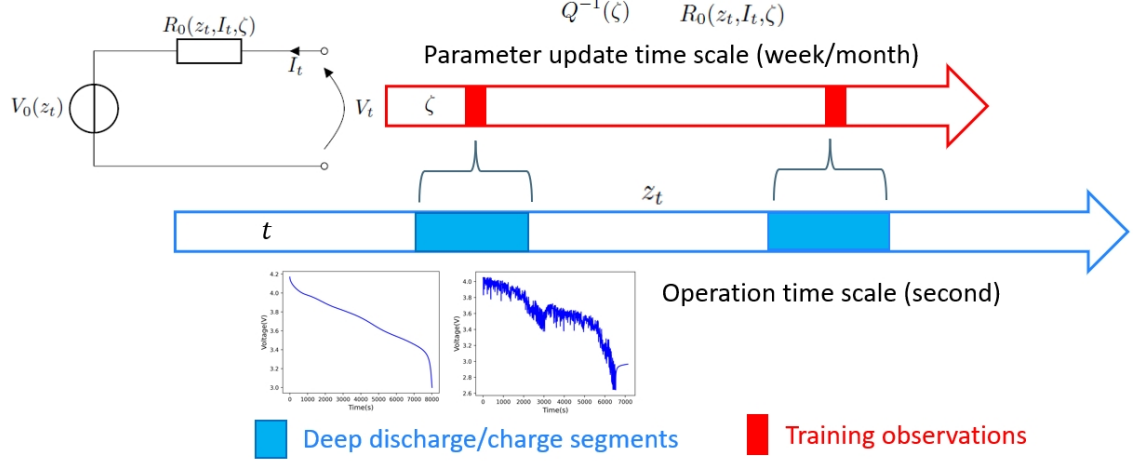


Fig. 2. Overview of combining battery operating dynamics and aging dynamics

scale. Because of the operating condition dependency of R_0 , kronecker products are used to describe corresponding discretisation in $\mathbf{I}_{n_s} \otimes \mathbf{F}_{WV}$ and \mathbf{w}_{j-1} . In this work, $n_s = n_z \cdot n_I$. Specifically, the 0 to 1 SOC range is evenly divided into n_z discrete SOC levels, while the applied current range (in absolute scale) is evenly divided into n_I discrete current levels. The process noise terms w_{j-1} and \mathbf{w}_{j-1} can be calculated following Eqn. 11, where Q_c for WV kernel is σ_ζ^2 .

While the forward propagation in these two subsystems are in different time scales (Δt_i and $\Delta \zeta_j$), terminal voltage (V_i) is the only available observation for both ECM and GPs. Preprocessing of voltage measurements is needed to reflect our consideration for these two different time scales. As shown in Fig. 2, charge/discharge segments are extracted from raw data, while the within segment time interval is Δt_i , and the between segment time interval is $\Delta \zeta_j$.

2.3 Joint estimation of battery states and GPs

For simplicity, the state covariance initialisation and process noise matrix of the joint system and GPs subsystem are summarized below,

$$\mathbf{P}_{\text{joint},0} = \begin{bmatrix} \mathbf{P}_{z,0} & 0 \\ 0 & \mathbf{P}_{\text{GP},0} \end{bmatrix}, \mathbf{P}_{\text{GP},0} = \begin{bmatrix} \mathbf{P}_{Q^{-1},0} & 0 \\ 0 & \mathbf{P}_{R_0,0} \end{bmatrix}$$

$$\mathbf{W}_{\text{joint}} = \begin{bmatrix} \mathbf{W}_z & 0 \\ 0 & \mathbf{W}_{\text{GP}} \end{bmatrix}, \mathbf{W}_{\text{GP}} = \begin{bmatrix} \mathbf{W}_{Q^{-1}} & 0 \\ 0 & \mathbf{W}_{R_0} \end{bmatrix} \quad (20)$$

where,

$$\mathbf{P}_{R_0,0} = \mathbf{K}_{\text{Mat}} \otimes \mathbf{P}_{\zeta_0, \text{WV}}, \quad \mathbf{P}_{Q^{-1},0} = \mathbf{P}_{\zeta_0, \text{WV}} \quad (21)$$

$$\mathbf{W}_{R_0} = \mathbf{K}_{\text{Mat}} \otimes \mathbf{W}_{\text{WV}}, \quad \mathbf{W}_{Q^{-1}} = \mathbf{W}_{\text{WV}}$$

where, ζ_0 represents the initial aging time step. \mathbf{K}_{Mat} is the covariance matrix of Matern kernel on n_z discrete SOC levels. And for the selected WV kernel, the initial covariance and noise matrix are given as,

$$\mathbf{P}_{\zeta_0, \text{WV}} = \sigma_z^2 \begin{bmatrix} \frac{1}{3} \zeta_0^3 & \frac{1}{2} \zeta_0^2 \\ \frac{1}{2} \zeta_0^2 & \zeta_0 \end{bmatrix}, \mathbf{W}_{\text{WV}} = \sigma_z^2 \begin{bmatrix} \frac{1}{3} \Delta \zeta^3 & \frac{1}{2} \Delta \zeta^2 \\ \frac{1}{2} \Delta \zeta^2 & \Delta \zeta \end{bmatrix} \quad (22)$$

In literature, many works (Hu et al., 2012; Wassiliadis et al., 2018) use a dual estimation framework which separately propagate these two subsystems, and use the estimated SOC (z) as the observation for parameter updating. One major drawback for this approach is the parameter estimation performance is largely depends on SOC accuracy. And by decoupling state from parameters any cross-correlations between the two are lost, which may lead to poor estimation accuracy (Plett, 2015). For example, the uncertainty information of SOC estimation, which matters to parameter update, is discarded in this process. On the other hand, many works (Liu et al., 2020; Yu et al., 2017) adopt a joint estimation framework which use operating time scale to update both states and parameters. These methods may suffer from poor numeric conditioning due to the vastly different time scales of the states and parameters. (i.e. the difference between seconds and months)

To mitigate problems mentioned above, we adopted a special co-estimation framework proposed in our former works (Aitio and Howey, 2021). Within segments, GPs states (i.e. parameters) and the ECM state are propagated jointly. While, between segments, only GPs states are propagated and the ECM state is reinitialized at the beginning of every segment. In this way, both GPs and ECM subsystems share same observations (i.e. eqn. 12), while their propagation are in different time scales.

Within a segment, the overall joint state vector of both ECM and GPs is given by,

$$\mathbf{x}_{\text{joint},i} = \begin{bmatrix} z_i \\ \mathbf{x}_{Q^{-1},i} \\ \mathbf{x}_{R_0,i} \end{bmatrix} \quad (23)$$

While, between segments, the GP subsystem is linear, and the GP state vector is given by,

$$\mathbf{x}_{\text{GP},j} = \begin{bmatrix} \mathbf{x}_{Q^{-1},j} \\ \mathbf{x}_{R_0,j} \end{bmatrix} \quad (24)$$

Notice that, within a segment, the joint system of GPs and ECM is nonlinear. The equations in Eqn. 12 is nonlinear in SOC(z_t) due to $V_0(z_t)$ and $R_0(z_t)$. For simplicity, we can write the nonlinear joint system dynamics into,

$$\mathbf{x}_{\text{joint},i} = g(\mathbf{x}_{\text{joint},i-1}, I_{i-1}, \mathbf{W}_{\text{joint},i-1})$$

$$V_i = h(\mathbf{x}_{\text{joint},i}, I_{i-1}, v_i) \quad (25)$$

Thus, extended Kalman filter is used to locally linearise the joint system and give corresponding Jacobian matrices,

$$\mathbf{G}_i = \frac{dg}{d\mathbf{x}_{\text{joint},i}}, \quad \mathbf{H}_i = \frac{dh}{d\mathbf{x}_{\text{joint},i}} \quad (26)$$

After introducing all required terms, the detailed co-estimation framework is shown in Alg.1. As R_0 is modelled with a GP, the predictive variance of R_0 need to be included when calculating the noise covariance of output (i.e. $I_i^2 \Sigma_{R_0,i}$ term in \mathbf{S}_i). Detailed derivations can be found in Appendix A and B.

Algorithm 1 Co-estimation for battery state and GPs using Extended Kalman filter. The NLML(Φ) is calculated recursively on every terminal voltage measurement.

- 1: **Initialisation at** $\zeta = \zeta_0$
 - 2: $\mathbf{x}_{\text{GP}}^+ = \mathbf{x}_{\text{GP},0}, \mathbf{P}_{\text{GP}}^+ = \mathbf{P}_{\text{GP},0}$
 - 3: $\Phi = 0$
 - 4: **for** $\text{seg}_j \in \text{segments}$ **do**
 - 5: **GP propagation**
 - 6: $\mathbf{x}_{\text{GP},j}^- = \exp(\mathbf{F}\Delta\zeta_j)\mathbf{x}_{\text{GP},j-1}^+$
 - 7: $\mathbf{P}_{\text{GP},j}^- = \exp(\mathbf{F}\Delta\zeta_j)\mathbf{P}_{\text{GP}}^+ \exp(\mathbf{F}\Delta\zeta_j)^T + \mathbf{W}_{\text{GP}}(\Delta\zeta_j)$
 - 8: **Initialisation at start of** j **th segment**
 - 9: $\mathbf{x}_{\text{joint}}^+ = \mathbf{x}_{\text{joint},0} = [z_0, \mathbf{x}_{\text{GP},j}^-]^T$
 - 10: $\mathbf{P}_{\text{joint}}^+ = \mathbf{P}_{\text{joint},0} = \begin{bmatrix} \mathbf{P}_{z,0} & 0 \\ 0 & \mathbf{P}_{\text{GP},j}^- \end{bmatrix}$
 - 11: **for** $V_i \in \text{seg}_j$ **do**
 - 12: **Joint states propagation**
 - 13: $\mathbf{x}_{\text{joint},i}^- = g(\mathbf{x}_{\text{joint},i-1}^+, I_{i-1}, \mathbf{W}_{\text{joint},i-1})$
 - 14: $\mathbf{P}_{\text{joint},i}^- = \mathbf{G}_{i-1}\mathbf{P}_{\text{joint},i-1}^+\mathbf{G}_{i-1}^T + \mathbf{W}_{\text{joint},i-1}$
 - 15: **Joint states update**
 - 16: $\mathbf{e}_i = V_i - h(\mathbf{x}_{\text{joint},i}^-, I_{i-1}, v_i)$
 - 17: $\mathbf{S}_i = \mathbf{H}_i\mathbf{P}_{\text{joint},i}^-\mathbf{H}_i^T + I_i^2\Sigma_{R_0,i} + \sigma_v^2$
 - 18: $\mathbf{L}_i = \mathbf{P}_{\text{joint},i}^-\mathbf{H}_i^T\mathbf{S}_i^{-1}$
 - 19: $\mathbf{x}_{\text{joint},i}^+ = \mathbf{x}_{\text{joint},i}^- + \mathbf{L}_i\mathbf{e}_i$
 - 20: $\Phi = \Phi + \frac{1}{2}\mathbf{e}_i^T\mathbf{S}_i^{-1}\mathbf{e}_i + \frac{1}{2}\log|2\pi\mathbf{S}_i|$
 - 21: **end for**
 - 22: **end for**
-

3. DATA PREPROCESSING

3.1 Data description

Cell A Cell A is a nickel-manganese-cobal (NMC)/graphite battery from an open dataset (Thelen et al., 2023). It is a commercial 502030 size NMC cell with nominal capacity of 250 mAh, operating voltage ranges from 3.0 to 4.2 V. However, it is found the initial of life capacity is around 280 mAh. And the beginning-of-life(BoL) DC resistance is around 130 m Ω . This battery is aged under repeated charge/discharge cycles with a weekly reference performance test(RPT). The cycling aging was conducted with constant 1.825C charging C-rate and constant 0.5C discharging C-rate. While the depth of discharge (DoD) is 100% and environmental temperature is kept at 30 $^\circ$ C. Considering the computation cost, we set the operating condition discretization for cell A as $n_z = 25$ and $n_I = 1$.

The RPT consists of a low C-rate (0.2C) constant current constant voltage (CC-CV) charging and constant current discharging, which gives ground truth discharge capacity

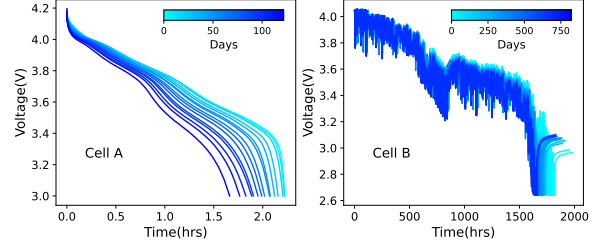


Fig. 3. Visualization of extracted discharge segments for Cell A and Cell B

and an up-to-date pseudo OCV-SOC curve. This cell number is G37C2 in the original dataset.

Cell B Cell B is a nickel-cobalt-aluminum oxide Li-ion battery from another open dataset with cell number 015 (Jöst et al., 2021). It is a commercial 18650 NCA/C+Si cell with nominal capacity of 3400 mAh. And the BoL DC resistance is around 25 m Ω . This battery is charged with a CC-CV regime and discharged using a scaled drive cycle profile. This scaled drive cycle profile covers a range from 0 to 9.7 A (absolute value). The cycle ageing was conducted at a temperature of 25 $^\circ$ C between 10% and 90% SOC. For cell B, we set the operating condition discretization as $n_z = 25$ and $n_I = 5$.

Regular RPTs are operated every 30 cycles with 0.1C current, which gives ground truth discharge capacity and an up-to-date pseudo OCV-SOC curve.

3.2 Extract discharge segments from cycling data

The sampling frequency for cycling is 0.2 Hz and 1 Hz for Cell A and B respectively. As a result, the corresponding entire lifelong cycling data consists of 1840632 and 41346756 rows of I, V . Using the entire cycling life data to estimate/optimize GP hyper-parameters require substantial computational effort. On the other hand, considering the purpose of battery SOH estimation, it is reasonable to neglect the aging effect between two adjacent cycles and only maintain small number of cycling segments with relative large between-segment time distances.

In this work, 15 and 18 discharge segments are extracted evenly across battery cycling life for cell A and B (in the sense of total cycle number), which reduces the data volume into 21881 and 120801 rows of I, V respectively. In practice, the time interval between segments can be adjusted regards of usage conditions. For example, in a fast aging test environment, one may choose an interval of 1 day, while in a field energy storage system, one may choose an interval of 1 month. The first 10 segments are used to train the proposed model. (i.e. optimize the kernel hyper-parameters for GPs). While only the RPT data at BoL is used to calibrate OCV-SOC relationship. The extracted discharge segments for Cell A and B are shown in Fig. 3. The aging effect can be clearly seen from the shrinkage of discharge curve on the time axis.

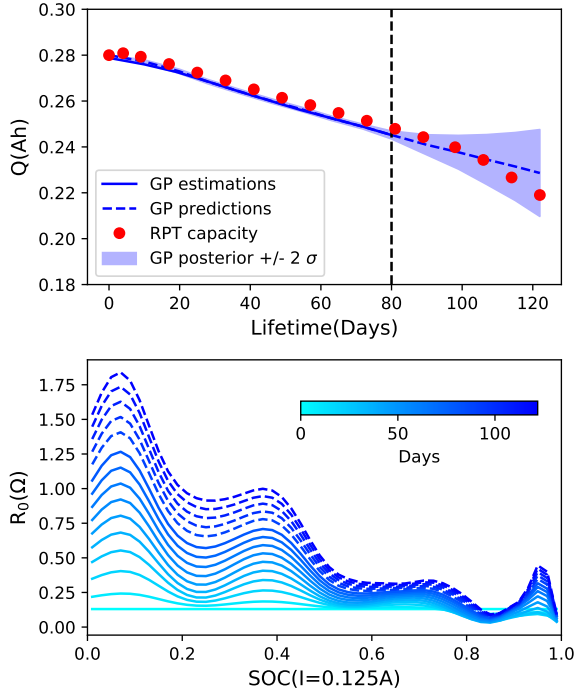


Fig. 4. Projections of GP posteriors for Q and R_0 of cell A. The ground truth RPT tests are only used as validations for capacity (red dots).

4. RESULTS AND DISCUSSION

4.1 SOH estimation

Fig. 4 and Fig. 5 show 1-D projections of the GP estimations of discharge capacity Q and operando impedance R_0 over battery lifetime for cell A and B respectively. The train-test-split is shown as the vertical black line in the bottom subplot. For Cell A, the discharge current is constant, thus, R_0 is only plotted against SOC. While for Cell B with dynamic discharging profile, R_0 is plotted against both SOC and the applied current.

It is clear that the GP captures the aging trend for capacity quite well based only on cycling data without RPTs. As the non-stationary WV kernel is used for modelling time dependency of $Q^{-1}(\zeta)$, the extrapolation of GP maintains the last known aging trend of the training stage. This linear extrapolation fits well for cell B, while it appears slightly worse for cell A as the ground truth aging speed accelerates. The uncertainty for estimations are shown as shaded area, which grows much larger when extrapolating into later future.

For the estimation results of R_0 , a clear upwards shift can be found for cell A, which indicates a systematic increase of battery impedance over all SOC levels along aging. While for cell B, R_0 changes in a more complex way where both increasing and decreasing trends can be found against different SOC levels. Also, compared to SOC levels, the scale of R_0 dependency on applied current is much smaller. Thus, we mainly discuss the SOC dependency in this work, more details about applied current dependency can be found in Appendix C.

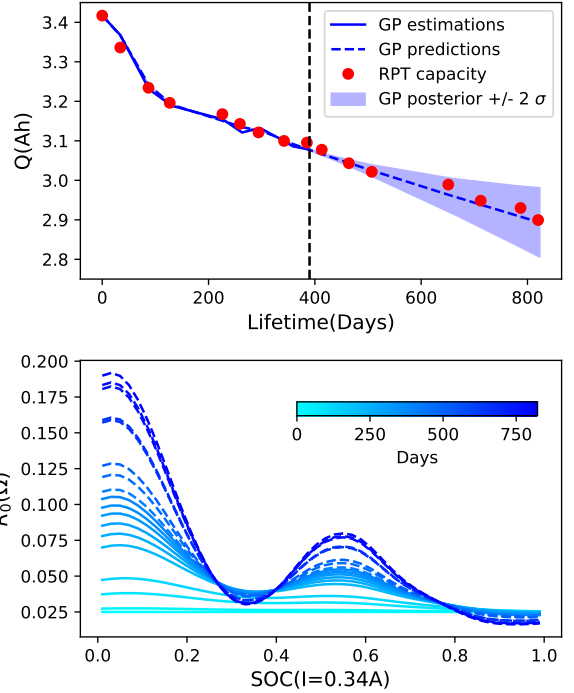


Fig. 5. Projections of GP posteriors for Q and R_0 of cell B. The ground truth RPT tests are only used as validations for capacity (red dots).

All estimations are shown in solid lines, extrapolations are shown as dot lines. The blue gradient colors denote the corresponding aging times. The extrapolation for R_0 also maintains the increasing trend of training stage. To keep the figure simple, the uncertainty for R_0 estimations are included in Fig. 6.

Notice that, in order to gain smoothness for estimated R_0 functions, the discretization of SOC is further increased into 100 evenly spaced locations. Then, the trained model reruns in a forward mode with learnt GP hyper-parameters, while it is now based on an extended SOC discretization.

4.2 SOC dependency analysis

There are two abnormal things for the impedance $R_0(z, \zeta)$ evolution. One is the increasing scale of R_0 is much larger than one would expected. Given that the BoL DC resistance calculated from pulse test is around 0.13Ω and 0.025Ω for cell A and B respectively, the large increase of R_0 (nearly 5 times level) in low SOC level is too large

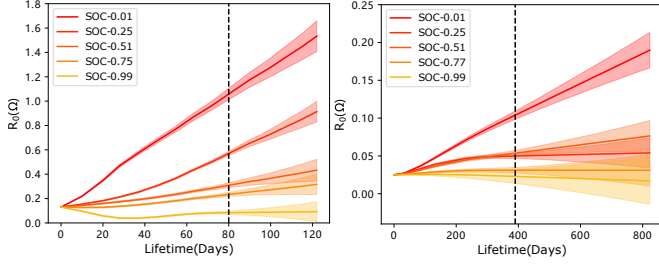


Fig. 6. The GP estimation of impedance increase on different SOC levels

to only reflect increase of resistance. Another eye-catching point is the wave-like curve shape and the corresponding unevenly increase against SOC. This SOC dependency of impedance is also observed by many other scholars (Waag et al., 2013; Schönleber et al., 2017). Fig. 6 further shows impedance increases across different SOC levels. In the training set, the increase at high SOC (> 0.9) are almost negligible for both cell A and B. While for low SOC (< 0.1), the increases of R_0 are nearly 0.88Ω and 0.07Ω for cell A and B respectively.

Considering these abnormal trends and our understanding of ECM, we propose that, a major part of estimated $R_0(z, \zeta)$ increase comes from the shape change of battery OCV-SOC curve. Specifically, the battery dynamic in Eqn.12 is under the assumption that the OCV-SOC relationship is kept the same across the whole battery life regardless of aging influence. A more realistic formulation should can be expressed as,

$$V_t = V_0(z_t, \zeta) + \hat{R}_0(z_t, \zeta)I_t \quad (27)$$

where the OCV-SOC relationship $V_0(z_t, \zeta)$ is itself a function of both SOC (z_t) and aging lifetime (ζ). And \hat{R}_0 is the pure impedance term. By further separate the OCV term into a fixed part $\bar{V}_0(z_t, \zeta_0)$ (BoL OCV-SOC) and an aging sensitive changing part $\Delta V_0(z_t, \zeta)$, one can further write this equation into,

$$V_t = \bar{V}_0(z_t, \zeta_0) + \Delta V_0(z_t, \zeta) + \hat{R}_0(z_t, \zeta)I_t$$

$$V_t = \bar{V}_0(z_t) + I_t \underbrace{\left[\frac{\Delta V_0(z_t, \zeta)}{I_t} + \hat{R}_0(z_t, \zeta) \right]}_{R_0(z_t, \zeta)} \quad (28)$$

It is now clear that, rather than pure impedance response \hat{R}_0 , the learnt impedance function $R_0(z_t, \zeta)$ consists of the influence from both OCV-SOC curve and impedance.

Thanks to the regular RPT data, we are able to validate above hypothesis with ground-truth OCV-SOC changes. Fig. 7 shows the comparison between the learnt $R_0(z_t, \zeta)$ and ground-truth OCV-SOC curves. Notice that, the applied current is 0.125A and 0.34A for cell A and B respectively. ΔOCV represents the difference between up-to-date OCVs and the BoL OCVs across all SOC levels. A great consistency can be observed for the changing trends of R_0 and OCV-SOC. And the Pearson linear coefficient is used for further quantitative description of this consistency. Specifically, for every discrete SOC value, the linear coefficient between R_0 increase and ΔOCV increase is calculated. For cell A, a linear coefficient more than 0.8 can be observed across all SOC levels, while it decreases slightly around 0.8 SOC. For cell B, a linear coefficient more than 0.7 can be

found for most SOC levels, while it decreases around 0.8 SOC.

One remaining issue is the identifiability between $\Delta V_0(z_t, \zeta)$ and $\hat{R}_0(z_t, \zeta)$. Given the additive nature for these two elements, it is impossible to distinguish them from terminal voltage measurements under this simple ECM structure. However, the differences of their influences on terminal voltage can be compared. Specifically, in our case, $I_t = 0.1235/0.34\text{A}$ for cell A and B, assume an aggressive 50% increase for BoL DC resistance, it only gives around $0.008/0.004\text{V}$ terminal voltage changes. While the average lifelong changes for OCV-SOC are 0.03 and 0.02V for cell A and B respectively.

4.3 Differential voltage analysis

While capacity decrease and impedance increase reflect SOH in a full cell level, these two metrics are not enough to further indicate different degradation mechanisms. One commonly used quantitative method is the differential voltage analysis (dV/dQ). The dV/dQ curve is obtained by differentiating discharge voltage with respect to cumulative discharge Ah. The peaks on the dV/dQ curve can be assigned to certain material phase transitions. The peak shifts and the changing between-peak distances are used to indicate different degradation modes, i.e. LLI, LAM_n and LAM_p (Dubarry and Anseán, 2022). One major limitation of dV/dQ method is its requirement for a low C-rate ($< C/20$) deep discharge, which is generally unavailable except for carefully controlled lab environment. Because of the experiment limits, the RPT C-rates for cell A and B are $C/5$ and $C/10$ respectively, we used it to get ground-truth dV/dQ curves.

Given the observed close relationship between $\Delta\text{OCV}(z, \zeta)$ and $R_0(z, \zeta)$, one natural extension is further comparing dV/dQ from RPTs and the learnt $d[I \cdot R_0]/dQ$. As shown in Fig. 8, multiply SOC with the learnt $Q(\zeta^*)$, one can substitute the dependency on SOC into corresponding discharge Ah and thus observe the shifting effects for its peaks.

Due to the lack of half cell test data, we are not able to attribute each peak of dV/dQ into its corresponding electrode, thus can not directly calculate LLI, LAM_n and LAM_p . But, quantitative analysis for shifts of peaks (P_1 , P_2 and P_3) are calculated and shown in Fig. 9. For both cells, the estimated peak shifts of $d[I \cdot R_0]/dQ$ covers similar ranges and changing trends compared to the ground-truth peak shifts of dV/dQ . While the divergence between estimations and ground truth of P_1 shifts are observed for cell A. The ground truth P_1 splitted into two peaks along aging, which is not captured in the $d[I \cdot R_0]/dQ$ estimations.

5. CONCLUSIONS

To achieve a more informative battery SOH estimations, we have proposed an aging-aware ECM, which incorporates GPs to describe the dependency of model parameters on SOC and aging time. A novel state space formulation is used to transform GPs into state space models and allows solving it in a linear time complexity with Kalman filter and RTS smoother. This also enables us to co-estimate

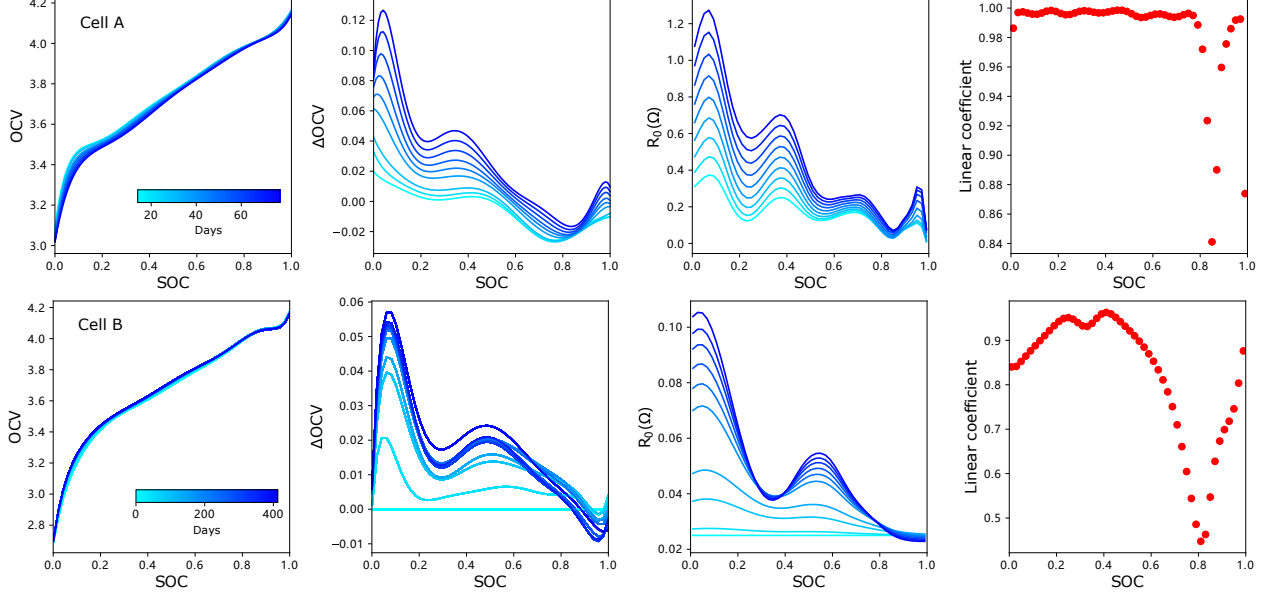


Fig. 7. Comparison between ground-truth OCV-SOC and the estimated R_0 function for cell A and B

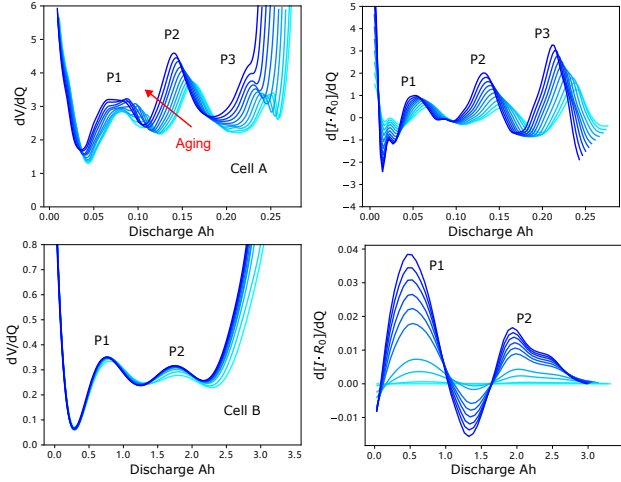


Fig. 8. The comparison between RPT dV/dQ and estimated $d[I \cdot R_0]/dQ$

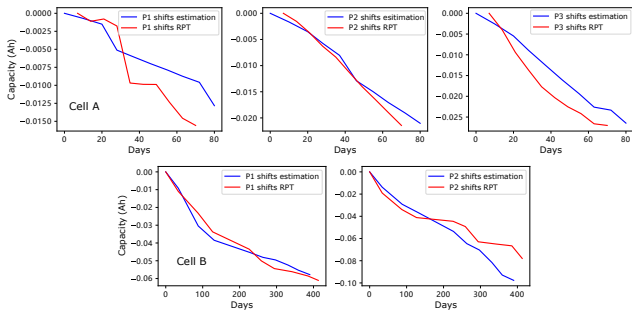


Fig. 9. Comparison of peak(P1,P2,P3) shifts for dV/dQ from RPTs and $d[I \cdot R_0]/dQ$ estimations.

both parameters and states in an unified framework based on extended Kalman filter. Comparing to random walks or deterministic models in existing literature, imposing GPs to modelling parameter evolution has multiple advantages:

- State space formulation of GP maintains gradient information of states while random walk/deterministic models do not.
- Incorporating SOC and aging time dependency of parameters by GP kernels makes ECM parameter estimations more stable across battery life, i.e. smoother interpolation and more reasonable extrapolation compared to random walk/deterministic models.
- A GP prior helps to mitigate numerical ill conditions, as it gives a regularisation effect when parameters are not easily identifiable (e.g. either caused by measurement noises or extrapolation into unseen conditions).

The estimation for capacity $Q(\zeta)$ shows great consistency with ground truth capacity from RPTs. While the estimations for impedance function show close relationship with the shape changes of OCV-SOC curve. We have shown a major part of learnt $R_0(z_t, \zeta)$ comes from OCV changes $\Delta V_0(z_t, \zeta)$. High linear coefficients (> 0.8) are observed between $R_0(z_t, \zeta)$ and $\Delta V_0(z_t, \zeta)$ among a wide range of SOC levels. By using both our estimations for $Q(\zeta)$ and $R_0(z_t, \zeta)$, we further calculate $d[I_t \cdot R_0]/dQ$ as estimations to ground truth dV/dQ curves. The estimated peak shifts of $d[I \cdot R_0]/dQ$ covers same value ranges and changing trends compared to the ground-truth peak shifts of dV/dQ .

For future work, the proposed model need to be further tested on cells under different working conditions, especially when the battery only go through shallow charging-discharging across life. Also, more detailed experiments and analysis are needed towards the identifiability between OCV changes and impedance response. Third, in principle, the state space formulation of GP can also be used in physics-based models which provides us with more physically explainable battery health estimations.

Appendix A. GAUSSIAN PROCESS WITH INPUT UNCERTAINTY

In the joint system dynamics of eqn. 25, R_0 needs to be evaluated in every step. Notice that, the SOC is itself a Gaussian distribution expressed as,

$$z_i \sim \mathcal{N}(z_i^-, \mathbf{P}_{z_i}^-) \quad (\text{A.1})$$

This means the R_0 is a GP with input uncertainty of z_i . the ordinary predictive distribution in eqn. 5 needs to be marginalised over z_i by taking the integral,

$$p(R_0) = \int p(R_0 | z_i) p(z_i) dz_i \quad (\text{A.2})$$

This integral is usually intractable and can be approximated using Taylor expansions (Girard et al., 2002), a first order expansion can be written as,

$$\begin{aligned} m_{R_0} &= K_{Z,z_i}^\top [K_Z + \sigma_{GP}^2 I]^{-1} z_i \\ \Sigma_{R_0} &= K_{z_i,z_i} - K_{Z,z_i}^\top [K_Z + \sigma_{GP}^2 I]^{-1} K_{Z,z_i} + \left. \frac{\partial R_0}{\partial z} \right|_{z_i}^\top \mathbf{P}_{z_i}^- \left. \frac{\partial R_0}{\partial z} \right|_{z_i} \end{aligned} \quad (\text{A.3})$$

Appendix B. PREDICTIVE VARIANCES FOR TERMINAL VOLTAGE

In the extended Kalman filter used for the GP and ECM joint system, one extra variance term $I_i^2 \Sigma_{R_0,i}$ is included in the calculation of \mathbf{S}_i . It corresponding to our consideration of R_0 uncertainty when calculating the predictive distribution of terminal voltage V_i ,

$$\begin{aligned} V_i &= V_0(z_i) + I_i R_{0,i} + \nu_i, \quad \nu_i \sim \mathcal{N}(0, \sigma_\nu^2) \\ \mathbb{E}[V_i] &= V_0(z_i) + I_i m_{R_0,i} \\ \text{cov}(V_i) &= \mathbb{E}[(V_i - \mathbb{E}[V_i])(V_i - \mathbb{E}[V_i])^\top] \\ \text{cov}(V_i) &= I_i^2 \Sigma_{R_0,i} + \sigma_\nu^2 \end{aligned} \quad (\text{B.1})$$

Appendix C. IMPEDANCE DEPENDENCY ON APPLIED CURRENT

REFERENCES

- Aitio, A. and Howey, D.A. (2021). Predicting battery end of life from solar off-grid system field data using machine learning. *Joule*, 5(12), 3204–3220.
- Berecibar, M., Gandiaga, I., Villarreal, I., Omar, N., Van Mierlo, J., and Van den Bossche, P. (2016). Critical review of state of health estimation methods of li-ion batteries for real applications. *Renewable and Sustainable Energy Reviews*, 56, 572–587.
- Cohen, L. (1998). The generalization of the wiener-khinchin theorem. In *Proceedings of the 1998 IEEE International Conference on Acoustics, Speech and Signal Processing, ICASSP'98 (Cat. No. 98CH36181)*, volume 3, 1577–1580. IEEE.
- Dubarry, M. and Anseán, D. (2022). Best practices for incremental capacity analysis. *Frontiers in Energy Research*, 10, 1023555.
- Dubarry, M., Truchot, C., and Liaw, B.Y. (2012). Synthesize battery degradation modes via a diagnostic and prognostic model. *Journal of power sources*, 219, 204–216.
- Feng, X., Weng, C., He, X., Han, X., Lu, L., Ren, D., and Ouyang, M. (2019). Online state-of-health estimation for li-ion battery using partial charging segment based on support vector machine. *IEEE Transactions on Vehicular Technology*, 68(9), 8583–8592.
- Fu, Y., Xu, J., Shi, M., and Mei, X. (2021). A fast impedance calculation-based battery state-of-health estimation method. *IEEE Transactions on Industrial Electronics*, 69(7), 7019–7028.
- Gao, Y., Liu, K., Zhu, C., Zhang, X., and Zhang, D. (2021). Co-estimation of state-of-charge and state-of-health for lithium-ion batteries using an enhanced electrochemical model. *IEEE Transactions on Industrial Electronics*, 69(3), 2684–2696.
- Girard, A., Rasmussen, C., Candela, J.Q., and Murray-Smith, R. (2002). Gaussian process priors with uncertain inputs application to multiple-step ahead time series forecasting. *Advances in neural information processing systems*, 15.
- Greenbank, S. and Howey, D. (2021). Automated feature extraction and selection for data-driven models of rapid battery capacity fade and end of life. *IEEE Transactions on Industrial Informatics*, 18(5), 2965–2973.
- Hu, C., Youn, B.D., and Chung, J. (2012). A multiscale framework with extended kalman filter for lithium-ion battery soc and capacity estimation. *Applied Energy*, 92, 694–704.
- Hua, Y., Liu, X., Zhou, S., Huang, Y., Ling, H., and Yang, S. (2021). Toward sustainable reuse of retired lithium-ion batteries from electric vehicles. *Resources, Conservation and Recycling*, 168, 105249.
- Jöst, D., Blömeke, A., Sauer, D.U., and Ringbeck, F. (2021). Timeseries data of a drive cycle aging test of 28 high energy nca/c+ si round cells of type 18650. Technical report, Institut für Stromrichtertechnik und Elektrische Antriebe.
- Li, T., Zhou, Z., Thelen, A., Howey, D.A., and Hu, C. (2024). Predicting battery lifetime under varying usage conditions from early aging data. *Cell Reports Physical Science*, 5(4).
- Li, W., Sengupta, N., Dechent, P., Howey, D., Annaswamy, A., and Sauer, D.U. (2021). Online capacity estimation of lithium-ion batteries with deep long short-term memory networks. *Journal of power sources*, 482, 228863.
- Li, Y., Liu, K., Foley, A.M., Zülke, A., Berecibar, M., Nanini-Maury, E., Van Mierlo, J., and Hoster, H.E. (2019). Data-driven health estimation and lifetime prediction of lithium-ion batteries: A review. *Renewable and sustainable energy reviews*, 113, 109254.
- Li, Y., Zou, C., Berecibar, M., Nanini-Maury, E., Chan, J.C.W., Van den Bossche, P., Van Mierlo, J., and Omar, N. (2018). Random forest regression for online capacity estimation of lithium-ion batteries. *Applied energy*, 232, 197–210.
- Liu, B., Tang, X., and Gao, F. (2020). Joint estimation of battery state-of-charge and state-of-health based on a simplified pseudo-two-dimensional model. *Electrochimica Acta*, 344, 136098.
- Locorotondo, E., Cultrera, V., Pugi, L., Berzi, L., Pierini, M., and Lutzemberger, G. (2021). Development of a battery real-time state of health diagnosis based on fast impedance measurements. *Journal of Energy Storage*, 38, 102566.

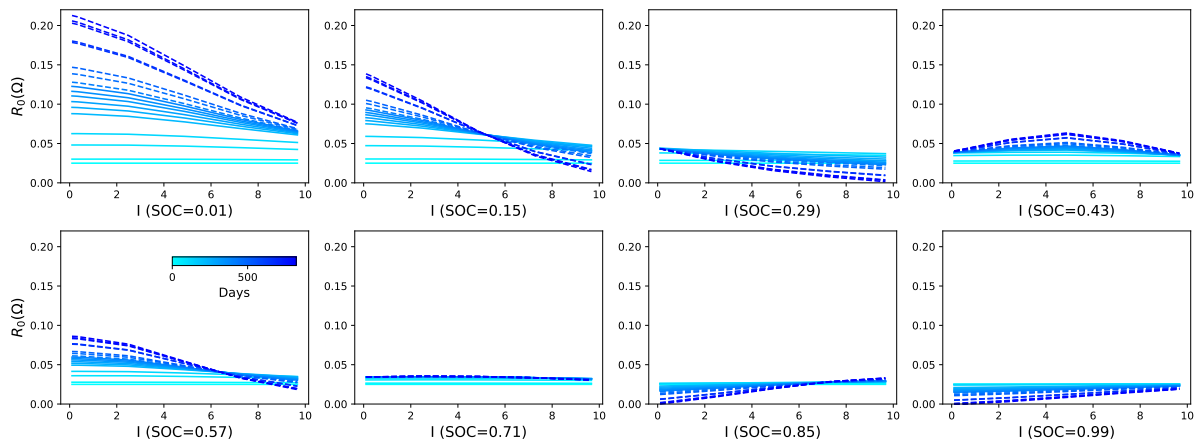


Fig. B.1. Impedance dependency on applied current for cell A

- Lu, D., Trimboli, M.S., Fan, G., Zhang, R., and Plett, G.L. (2021). Implementation of a physics-based model for half-cell open-circuit potential and full-cell open-circuit voltage estimates: part i. processing half-cell data. *Journal of The Electrochemical Society*, 168(7), 070532.
- Miguel, E., Plett, G.L., Trimboli, M.S., Oca, L., Iraola, U., and Bekaert, E. (2021). Review of computational parameter estimation methods for electrochemical models. *Journal of Energy Storage*, 44, 103388.
- Plett, G.L. (2004). Extended kalman filtering for battery management systems of lipb-based hev battery packs: Part 3. state and parameter estimation. *Journal of Power sources*, 134(2), 277–292.
- Plett, G.L. (2015). *Battery management systems, Volume II: Equivalent-circuit methods*. Artech House.
- Pozzato, G., Allam, A., Pulvirenti, L., Negoita, G.A., Paxton, W.A., and Onori, S. (2023). Analysis and key findings from real-world electric vehicle field data. *Joule*, 7(9), 2035–2053.
- Richardson, R.R., Birkl, C.R., Osborne, M.A., and Howey, D.A. (2018). Gaussian process regression for in situ capacity estimation of lithium-ion batteries. *IEEE Transactions on Industrial Informatics*, 15(1), 127–138.
- Sarkka, S., Solin, A., and Hartikainen, J. (2013). Spatiotemporal learning via infinite-dimensional bayesian filtering and smoothing: A look at gaussian process regression through kalman filtering. *IEEE Signal Processing Magazine*, 30(4), 51–61.
- Särkkä, S. and Svensson, L. (2023). *Bayesian filtering and smoothing*, volume 17. Cambridge university press.
- Schönleber, M., Uhlmann, C., Braun, P., Weber, A., and Ivers-Tiffée, E. (2017). A consistent derivation of the impedance of a lithium-ion battery electrode and its dependency on the state-of-charge. *Electrochimica Acta*, 243, 250–259.
- Severson, K.A., Attia, P.M., Jin, N., Perkins, N., Jiang, B., Yang, Z., Chen, M.H., Aykol, M., Herring, P.K., Fraggedakis, D., et al. (2019). Data-driven prediction of battery cycle life before capacity degradation. *Nature Energy*, 4(5), 383–391.
- Shahjalal, M., Roy, P.K., Shams, T., Fly, A., Chowdhury, J.I., Ahmed, M.R., and Liu, K. (2022). A review on second-life of li-ion batteries: Prospects, challenges, and issues. *Energy*, 241, 122881.
- Solin, A. et al. (2016). *Stochastic differential equation methods for spatio-temporal Gaussian process regression*. Ph.D. thesis, Aalto University.
- Sulzer, V., Mohtat, P., Aitio, A., Lee, S., Yeh, Y.T., Steinbacher, F., Khan, M.U., Lee, J.W., Siegel, J.B., Stefanopoulou, A.G., et al. (2021). The challenge and opportunity of battery lifetime prediction from field data. *Joule*, 5(8), 1934–1955.
- Thelen, A., Li, T., Liu, J., Tischer, C., and Hu, C. (2023). Isu-ilcc battery aging dataset. <https://doi.org/10.25380/iastate.22582234.v2>. doi:10.25380/iastate.22582234.v2.
- Tsiropoulos, I., Tarvydas, D., Lebedeva, N., et al. (2018). *Li-ion batteries for mobility and stationary storage applications*. Publications Office of the European Union.
- Waag, W., Käbitz, S., and Sauer, D.U. (2013). Experimental investigation of the lithium-ion battery impedance characteristic at various conditions and aging states and its influence on the application. *Applied energy*, 102, 885–897.
- Wang, Y., Tian, J., Sun, Z., Wang, L., Xu, R., Li, M., and Chen, Z. (2020). A comprehensive review of battery modeling and state estimation approaches for advanced battery management systems. *Renewable and Sustainable Energy Reviews*, 131, 110015.
- Wassiliadis, N., Adermann, J., Frericks, A., Pak, M., Reiter, C., Lohmann, B., and Lienkamp, M. (2018). Revisiting the dual extended kalman filter for battery state-of-charge and state-of-health estimation: A use-case life cycle analysis. *Journal of Energy Storage*, 19, 73–87.
- Wei, J., Dong, G., and Chen, Z. (2017). Remaining useful life prediction and state of health diagnosis for lithium-ion batteries using particle filter and support vector regression. *IEEE Transactions on Industrial Electronics*, 65(7), 5634–5643.
- Williams, C.K. and Rasmussen, C.E. (2006). *Gaussian processes for machine learning*. MIT press Cambridge, MA.
- Yu, Q., Xiong, R., Lin, C., Shen, W., and Deng, J. (2017). Lithium-ion battery parameters and state-of-charge joint estimation based on h-infinity and unscented kalman filters. *IEEE Transactions on Vehicular Technology*, 66(10), 8693–8701.

Zhou, Z., Ran, A., Chen, S., Zhang, X., Wei, G., Li, B., Kang, F., Zhou, X., and Sun, H. (2020). A fast screening framework for second-life batteries based on an improved bisecting k-means algorithm combined with fast pulse test. *Journal of Energy Storage*, 31, 101739.